Mesoporous ZnS Thin Films Prepared by a Nanocasting Route

Achim Fischereder,[†,‡] Maria Luz Martinez-Ricci,[⊥,#] Alejandro Wolosiuk,[⊥] Wernfried Haas,[‡,§] Ferdinand Hofer,[§] Gregor Trimmel,[†,‡] and Galo J. A. A. Soler-Illia*[,⊥]

[†]Institute for Chemistry and Technology of Materials, Graz University of Technology, Stremayrgasse 9, 8010 Graz, Austria

[‡]Christian Doppler Laboratory for Nanocomposite Solar Cells, Graz University of Technology and NanoTecCenter Weiz Forschungsgesellschaft GmbH, Austria

[§]Institute for Electron Microscopy and Fine Structure Research, Graz University of Technology, Steyrergasse 17, 8010 Graz, Austria

[⊥]Gerencia Química, Centro Atómico Constituyentes Comisión Nacional de Energía Atómica, Avenida Gral Paz 1499, B1650KNA San Martín, Argentina

[#]DQIAQF, Universidad de Buenos Aires, Facultad de Ciencias Exactas y Naturales, Ciudad Universitaria Pab. II, C1428EHA Buenos Aires, Argentina

ⓈSupporting Information

ABSTRACT: Mesoporous metal chalcogenides (e.g., ZnS, CuS, and derived mixed sulfide or selenides) show an extremely high potential in technological areas like catalysis, sensors, environmental protection, and photovoltaics. Although chemical bath deposition methods allow obtaining stable and porous metal chalcogenide films under mild and simple conditions, the reproducible preparation of highly ordered mesoporous sulfide thin films has been challenging so far. Herein, we present a simple and efficient synthetic method to prepare ZnS mesoporous thin films using a combination of a nanocasting approach and a successive ionic layer adsorption and reaction (SILAR) process for the infiltration. A mesoporous silica thin film, prepared by evaporation induced self-assembly (EISA), serves as the hard exotemplate for the formation of the mesostructured zinc sulfide. After selective etching of the silica framework, a stable and porous ZnS thin film is obtained, which replicates the pore structure of the hard template. A thorough combination of characterization techniques is used to assess the exotemplating process as well as the template removal.

KEYWORDS: *zinc sulfide, mesoporous film, nanocasting, SILAR*
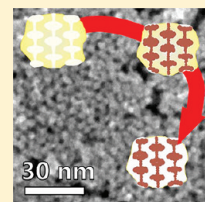
■ INTRODUCTION

Since the first reports concerning the preparation of three-dimensional ordered silica networks by supramolecular templating and coassembly, mesoporous materials have attracted a lot of scientific and industrial attention.[1,2] Because of their unique properties (monodisperse mesoporosity, highly ordered structure, accessible high surface area <2000 m^2 g^{-1}), the possibility to tailor their morphological parameters such as pore size and geometry and to functionalize the mesoporous materials, these materials find prospective applications in fields such as biomedicine, catalysis, environmental protection, optics, sensors or photovoltaics.[3-5] In addition to siliceous materials, mesoporous transition metal oxides, metals, carbons or metal chalcogenides can be prepared by combining the sol−gel process with surfactant templating.[6-8] However, in the case of nonsiliceous materials, the chemistry involved in the controlled building of the inorganic framework (solvolysis, condensation and/or redox reactions) is much more varied and the control is not straightforward.[9] In the particular case of metal sulfides, the necessity of favorable interactions between the surfactant template and the final mesoporous nanocrystalline material requires special attention. Sulfide ions must be generated in situ or slowly introduced as H$_2$S for a controlled precipitation of the metal sulfide within the templating structure.[10-12] Simultaneously, the competition between homogeneous and hetero-

geneous nucleation of semiconductor clusters must be thoroughly controlled in order to achieve the homogeneous formation of a semiconductor film, or its anchoring to colloidal surfaces.[13] In addition, the removal of the surfactant soft template without destroying the mesoporous structure turns out to be difficult, as the single nanoparticles are normally weakly bound to each other,[14] and oxidation reactions or fast, extended oxide crystallization might take place. Recently, high loading of transition metals salts in dual surfactant lyotropic liquid-crystalline phases allowed for synthesis of spongy mesostructured CdS/Se and ZnS/Se[15,16] films with thicknesses in the range of 400−600 nm. However, temperature must be carefully controlled in order to prevent both the lyotropic liquid crystalline phase destabilization and salt crystallization within the mesophases.

These synthetic issues can be easily solved using a nanocasting approach, in which mesoporous silica serves as a hard exotemplate.[17-20] This robust and universal synthetic method allows for the preparation of novel mesoporous materials (e.g., carbons, metals, nonoxidic phases), which cannot be prepared through sol−gel processes in a straightfor-

Scheme 1. Schematic Illustration of the Single Steps during the Infiltration of the MSF Substrate Using SILAR
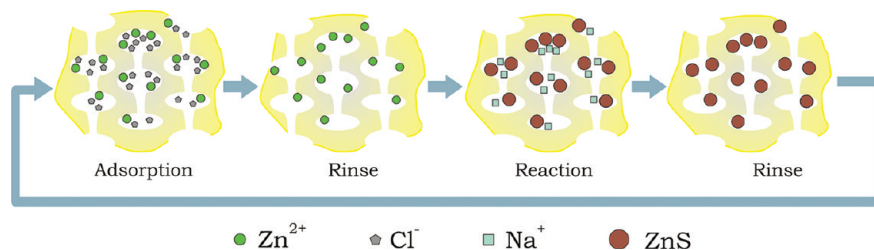
ward way.[21,22] After infiltration of the desired material or precursor within the nanospace provided by the pores of the hard silica template, further treatments can be carried out without the danger of destroying the meso-organized structure. Therefore, even high surface area inorganic compounds, which require high temperatures for their synthesis, can be obtained.[23] In addition, the interconnected three-dimensional pore structure of the mesoporous silica allows the formation of a continuous solid phase of the infiltrated nanomaterial. The selective removal of the silica template results in a stable nanostructured material, which is an inverse replica of the exotemplate.[24]

Several applications in catalysis, sensing, or solar cells require processing of nonoxide materials as mesoporous thin films (MTF). Indeed, a number of promising film applications for mesoporous metal chalcogenide coatings have been described in the sensing area; for example, pressed powders obtained from nanocasting have been used. Although the nanocasting method is well-established for bulk samples (i.e., monoliths or powders), it has been less developed for MTF.[21,22,25] In this context, the use of mesoporous chalcogenide thin films (i.e., ZnS, CdS, ZnSe, CIGS, etc.) for photovoltaic applications represent an interesting approach for the design of inorganic–organic hybrid solar cells. The high surface area of a mesoporous-based material would allow controlling the charge separation while keeping an efficient charge collection based on the connectivity to the underlying electrode. On the other hand, a direct film processing pathway, compatible with the electronics industry, is a desired feature for real devices, in order to minimize steps and keep reproducible, tailored porosity. In addition to the intrinsic MTF chemical stability, film–substrate adhesion, and the preservation of the substrate properties (i.e., conductivity, transparency, texture) are essential issues if optoelectronics applications in solar cells or sensors are sought for.

In this contribution, we focus on the synthesis and characterization of mesoporous ZnS thin films using a nanocasting approach. Mesoporous silica thin films prepared by an evaporation induced self-assembly method (EISA) are used as a hard template,[26] which is infiltrated, in a subsequent step, with ZnS by a successive ionic layer adsorption and reaction (SILAR) process.[27−29] The silica exotemplate is then selectively etched away to expose the stable mesoporous ZnS thin film. The steps of the preparation process as well as the final ZnS thin film are characterized using UV/vis, environmental ellipsometry porosimetry (EEP), scanning electron microscopy (SEM) including energy-dispersive X-ray spectroscopy (EDS) and transmission electron microscopy (TEM, bright field imaging and selected area electron diffraction, SAED). In addition, small-angle X-ray scattering (SAXS) and X-ray reflectometry (XRR) measurements were performed.

■ EXPERIMENTAL SECTION

Chemicals. Tetraethoxysilane (TEOS, 99.999%, trace metal basis), triblock copolymer Pluronics F-127 (F127, PEO_{106}-PPO_{70}-PEO_{106}, $M_W \approx 13\,800$), zinc(II) chloride ($ZnCl_2$, puriss. p. a.), sodium sulfide (Na_2S, 98%), hydrochloric acid (HCl, 37%, ACS reagent), and ethanol (EtOH, absolute) were purchased from Sigma Aldrich and used without further purification. Millipore water was used for the preparation of all precursor solutions.

Glass substrates were purchased from Marienfield (Germany) and indium tin oxide- (ITO)-coated glass substrates with a surface resistivity of 15–25 Ω/cm^2 were purchased from Delta Technologies Ltd. (USA).

Preparation of Mesoporous SiO_2 Thin Films. Mesoporous silica films (MSF) were prepared on ITO-covered glass (glass/ITO) substrates by a sol–gel method based on the oxide precursor tetraethoxysilane (TEOS) using Pluronic F-127 as templating agent. Samples were also deposited onto thin glass cover slips presenting a predeposited 80 nm thick ZrO_2 buffer layer (glass/ZrO_2); this buffer layer was prepared by dip-coating from a $ZrCl_4$/EtOH/water solution of molar composition 1:40:20, and subsequent firing to 350 °C. Prior to deposition, the substrates were washed with Dextran or other suitable surfactant-based cleaning agents, followed by rinsing with water and ethanol. Precursor films were prepared by dip-coating with a withdrawing speed of 4 mm s^{-1} under 40−50% relative humidity (RH) at room temperature. The precursor solution was prepared using the following molar ratios: 1 TEOS: 0.0055 F127: 40 EtOH: 10 H_2O: 0.009 HCl. Deposited films were stored immediately in a chamber with 50% RH for 30 min followed by a stabilizing thermal treatment of 30 min at 60 °C and 30 min at 130 °C. The final calcination was carried out at 350 °C for 2 h. After this treatment, robust and adhesive SiO_2 films with a well-defined mesoporous structure were obtained.

Infiltration of the Mesoporous SiO_2 Films. To infiltrate the mesoporous SiO_2 films with ZnS (MSF:ZnS), we used a successive ionic layer adsorption and reaction (SILAR) process. Each infiltration cycle consisted of four steps as represented in Scheme 1: in the first step the SiO_2 film is placed for 1 min in a 0.1 M aqueous solution of $ZnCl_2$. Zn(II) species are adsorbed on the silica surface, forming an electrical double layer with the Cl$^-$ anions. The surface adsorption of the Zn^{2+} ions takes place as long as the isoelectric point (i.e.p.) of the substrate (iep of $SiO_2 \approx 1.7−3.5$) is below the pH of the $ZnCl_2$ solution (pH 6.0). In the second step, the substrate is rinsed with distilled water to remove unadsorbed Zn^{2+} and Cl$^-$ ions from the diffuse layer. In the third step the substrate is immersed into a 0.07 M aq. Na_2S solution for 1 min leading to the replacement of the Cl$^-$ ions with S^{2-} ions. Hence, the reaction between the Zn^{2+} and S^{2-} ions occurs, leading to the formation of insoluble ZnS clusters. In the last step, the substrate is washed again with H_2O to remove Na_2S in excess. This cycle was repeated several times, in order to obtain higher pore loading with ZnS.

Characterization. UV–vis optical characterization of the films was performed with a Hewlett-Packard 8453 spectrophotometer. Environmental Ellipsometric Porosimetry (EEP) measurements were performed on a UV–visible (190−1000 nm, MgF_2 optics) variable angle spectroscopic ellipsometer (VASE) from SOPRA (GES5A), and analyzed with the WVase 32 software. Dynamic in situ monitoring of the film parameters (index of refraction and thickness) was realized by varying of the relative vapor pressures between 0% and 100% inside

the analysis chamber.[20] Field emission-scanning electron microscopy (FE-SEM) images were taken with a ZEISS LEO 982 GEMINI field emission electron microscope in the secondary-electron mode, using an in-lens detector to improve resolution. Energy-dispersive X-ray (EDS) spectra were recorded with a scanning electron microscope using a Philips SEM 515 equipped with a Falcon detector. Transmission electron microscopy (TEM) bright-field images were acquired on a Tecnai 20 microscope (FEI Company, 200 kV, LaB$_6$ cathode) and selected area electron diffraction (SAED) patterns were acquired on a Tecnai 12 microscope (FEI Company, 120 kV, LaB$_6$ cathode).

Film density was obtained from the analysis of the critical angle of X-ray Reflectometry (XRR) measurements that were performed at the D10A-XRD2 line of Laboratorio Nacional de Luz Sincrotron (LNLS), Campinas, SP, Brazil ($\lambda = 1.5498$ Å).[30] To obtain accurate density values, we completed measurements under dry nitrogen flux to avoid atmospheric water condensation within the pores which would lead to an underestimation of mesoporosity. The film mesostructure was analyzed using SAXS in transmission mode at the D11A-SAXS2 line of LNLS ($\lambda = 1.608$ Å) at normal and 3° incidence on thin glass covers.

■ RESULTS AND DISCUSSION

a. Characterization of MSF Exotemplate on ITO/ZrO$_2$ Substrates. Mesoporous silica film (MSF) exotemplates were prepared by an evaporation induced self-assembly (EISA) process using F127 as templating agent.[26] The preparation method involves dip-coating of substrates (glass/ITO or glass/ZrO$_2$) into the silica-based precursor solution described above under controlled atmosphere. After thermal stabilization treatment up to 350 °C, robust, transparent, and well-defined mesoporous silica films on ITO or glass were obtained.

Figure 1a shows the SEM image of the top layer of an MSF prepared on an ITO-covered glass substrate. The porous
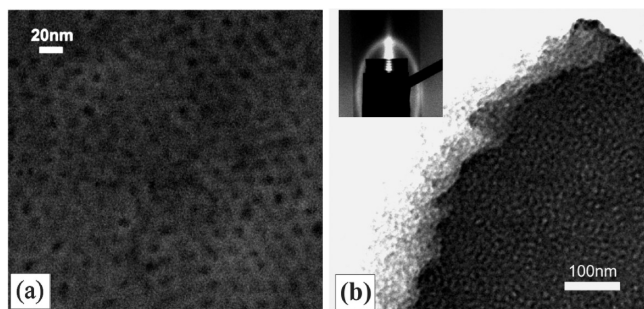

Figure 1. (a) SEM and (b) TEM images of a MSF patterned with F127. Inset in b shows a SAXS image at 3° incidence.

structure can be recognized with pore sizes of approximately 6 nm radius measured from the SEM image. Figure 1b shows a typical TEM image of the MSF, where it is possible to observe homogeneous mesopores with local order structure. Along the silica samples, regions presenting this kind of local pore order and Im3$\overline{m}$ structure are observed. The inset in Figure 1b corresponds to a 2D SAXS image of a MSF thin film over glass/ZrO$_2$, where the scattering pattern shows a continuous ellipsoidal figure, confirming the local order structure observed in the TEM image.[31]

Employing UV−VIS spectroscopic ellipsometry measurements in the range of 250 to 850 nm, it was possible to obtain the thickness and the refractive index of the MSF on glass/ITO. For this characterization, the Cauchy model for the index of refraction is suitable for both semiconductive layers (ITO and MSF) and the glass substrate.[32,33] This model expresses the functional dependence of the real and imaginary parts of the index of refraction with wavelength $n(\lambda) = n_r(\lambda) + in_i(\lambda)$, where the real part is expressed as

$$n_r(\lambda) = A + \frac{B}{\lambda^2} + \frac{C}{\lambda^4} \tag{1}$$

and the imaginary component as

$$n_i(\lambda) = \frac{D}{\lambda} + \frac{E}{\lambda^3} + \frac{F}{\lambda^5} \tag{2}$$

A, B, C, D, E, and F are parameters, whose value was adjusted according to the modeled material. In particular, in the case of transparent materials, $n_i(\lambda) = 0$ in the wavelength range studied.

Implementing this model to each layer of the system under study (MSF and ITO), the parameters obtained, using spectroscopic ellipsometry at 0% RH, are specified in Table 1. The first column refers to the thickness d of each layer. Refractive indexes for both films, obtained from the best fit of the ellipsometric parameters Ψ and Δ to the Cauchy parameters shown in Table 1 are plotted in Figure 2.
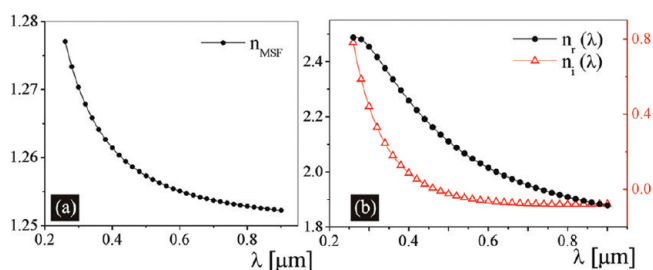

Figure 2. Refractive index curves corresponding to the parameters shown in Table 1: (a) MSF, (b) ITO layer (black circles and left axis correspond to $n_r(\lambda)$, red triangles and right axis correspond to $n_i(\lambda)$).

The Cauchy parameters for the mesoporous silica film show, as expected, that the MSF has no absorption (i.e., $n_i(\lambda) = 0$) and only two parameters are needed to properly fit the refractive index. This is not the case of the ITO layer, where six Cauchy parameters are necessary to get an appropriate index of refraction model. The last column of Table 1 shows typical refractive index values for both MSF and ITO layers at 630 nm.

The refractive index of MSF layers changes in the presence of vapors, due to the adsorption and condensation of molecules from the gas phase into the mesopores. The EEP technique uses this phenomenon to assess morphological parameters of the pore system, such as pore volume and pore and neck size distribution.[34] Due to pore filling with water, the MSF refractive index increases from 1.26 at lower vapor pressures to 1.43 at saturation. Using an effective medium model, and the

Table 1. Thickness and Optical Parameters of the Cauchy Model for the MSF and the ITO Layers for 250 nm < λ < 850 nm

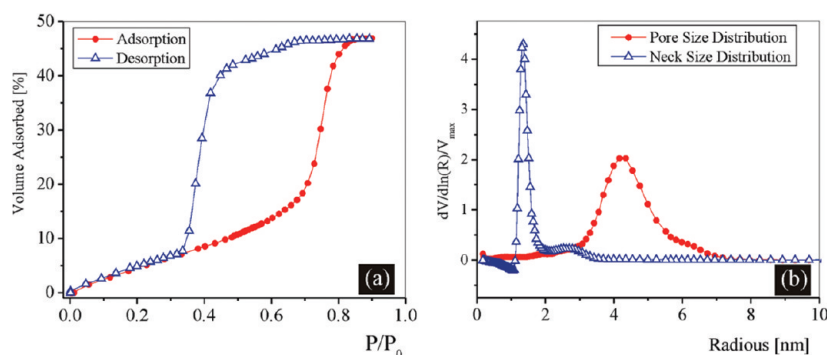|	d (nm)	A	B (μm²)	C (μm⁴)	D (μm)	E (μm³)	F (μm⁵)	n_{630}
MSF	202.9	1.25	1.83×10^{-3}					$1.26 + 0i$
ITO	159.5	1.76	0.103	-3.62×10^{-3}	-9.67×10^{-2}	2.15×10^{-2}	-8.89×10^{-5}	$1.99 - 4.31 \times 10^{-2}i$

Figure 3. (a) Adsorption−desorption isotherms and (b) pore and neck size distribution of a mesoporous SiO_2 thin film prepared on glass/ITO with F127 as surfactant.
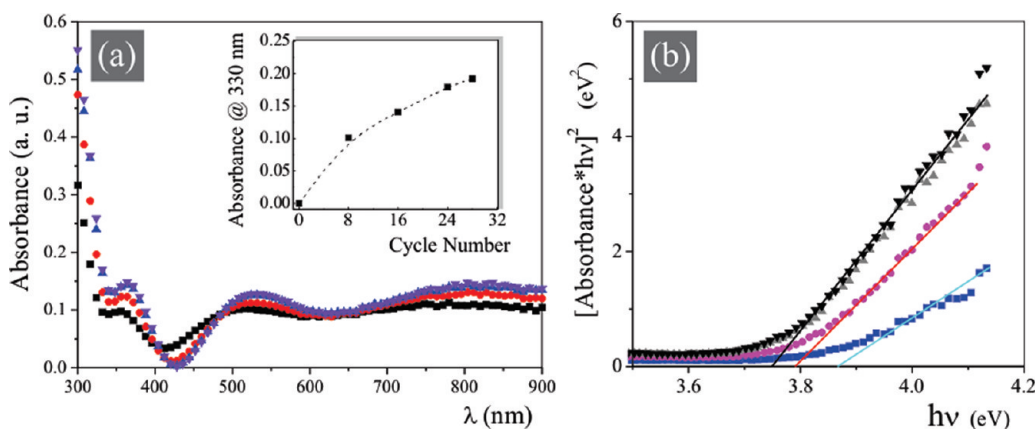

Figure 4. (a) Evolution of the absorption behavior of a MSF on glass/ITO during infiltration with ZnS. Inset: increase of absorption at 330 nm vs number of infiltration cycles (b) Tauc plot (i.e., $(\varepsilon h \nu)^2$ versus E of the incident light) of ZnS-MSF nanocomposites with variable sulphide loading (■ 8 cycles, ● 16 cycles, ▲ 24 cycles, ▼ 26 cycles); the linear fits at high energy permit to estimate the band gap for each sample.

values of refractive index of Table 1 as seeds, the adsorbed water volume can be calculated for all the range of vapor pressures. Figure 3a shows the adsorption−desorption isotherms obtained by applying this model to an MSF prepared on an ITO-covered glass substrate. The isotherms present Type IV behavior, showing a steep increase/decrease in adsorption/desorption due to capillary condensation, and H2 hysteresis loops, characteristic of cage-like mesopores with restrictions.[35] Figure 3a shows that the overall accessible porosity of the film is approximately 47%. The pore and neck size distribution can be calculated from the adsorption and desorption isotherms respectively. In mesoporous samples presenting H2 loops, pore sizes are obtained from adsorption the isotherm that reflects equilibrium, and the neck diameter can be obtained from the desorption curves.[36] The film exhibits pore and neck radii of around 4.5 and 1.3 nm respectively, based on the Kelvin equation[37,38] (Figure 3b), which is in excellent agreement with literature data[39] and the results obtained from the SEM image analysis (Figure 1).

b. ZnS Infiltration: Characterization of MSF:ZnS Nanocomposite Films. ZnS is a wide gap semiconductor with multiple applications such as light emitting diodes, IR windows, transparent conductive coatings, and solar cell buffer layers.[40] Controlled synthesis of ZnS within the pore system of the MSF exotemplate was performed using the SILAR process described in the Experimental Section and illustrated in Scheme 1. Alternate immersion of the film in solutions of a metal salt,

$ZnCl_2$, and a sulfur source, Na_2S is used to grow the semiconductor crystals in subnanometer steps.[19,41]

This simple approach allows a controlled ZnS infiltration within the SiO_2 exotemplate although there is a competition between this process and the nucleation of ZnS clusters on the external surface of the MSF. Nonetheless, this issue can be minimized working with dilute ZnS precursor solutions, as described in this work.

UV/vis spectroscopy was employed in order to track the MSF infiltration with ZnS in each SILAR cycle, as shown in Figure 4a. A significant increase of the absorption below 340 nm is observed due to the formation of ZnS (typical band gap ZnS 3.6−3.8 eV). The shift in the absorption fringes appears because the total optical path changes at each ZnS infiltration step due to the variation in the refractive index of the film matrix as the ZnS fills the mesopores.

The band gap of MSF:ZnS composites with different ZnS loading was obtained by plotting the data as the well-known Tauc plot, i.e., $(\varepsilon h \nu)^2$ versus the energy of the incident light in eV, $h\nu$. After extrapolation of the linear region to zero, a steady decrease in the E_g from 3.86 to 3.75 eV is observed as infiltration proceeds.[42] These values are well above the E_g bulk values for cubic ZnS, 3.6 eV and hexagonal ZnS, 3.8 eV.[43] Independently of the ZnS crystalline phase present in the nanocomposites, it is clear that as the ZnS nanoparticles grow with each infiltration step, the observed E_g converges to the bulk value. Interestingly, after 24 SILAR cycles, the optical

absorption seems to reach a plateau (inset in Figure 4a), suggesting that ZnS infiltration reaches an upper limit.

The infiltration process is clearly observed by electron microscopy. Comparing SEM micrographs along the MSF films before and after 28 cycles of infiltration (Figure 5), it is evident
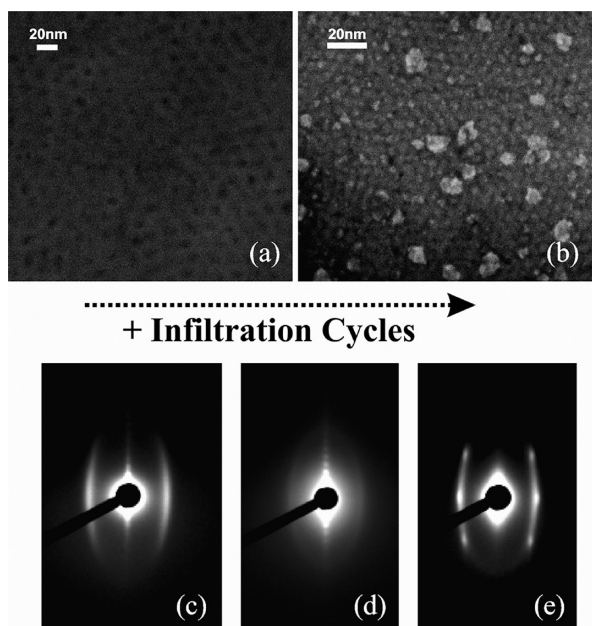

Figure 5. SEM images of a MSF prepared on glass/ITO (a) before infiltration and (b) after 28 cycles of infiltration. SAXS images of a MSF on glass/ZrO₂ for: (c) 0, (d) 14, and (e) 28 cycles.

that, at least, surface pores or walls are filled with ZnS. In particular, SiO₂ pores that appear as dark spots in Figure 5a turn white as they are filled with ZnS, as shown in Figure 5b. This change in the image intensity is caused by the fact that heavy elements (e.g., Zn) produce more secondary electrons than lighter elements (e.g., Si). Therefore, in SEM images, regions containing heavier elements appear brighter than regions with lighter elements. This result demonstrates that the SILAR process leads to a uniform infiltration of the mesoporous structure with ZnS.

The same qualitative trend is observed when analyzing SAXS patterns of empty and infiltrated MSF. Mesoporous silica samples on ITO display continuous ellipsoidal diffraction patterns corresponding to a mixture of an $Im3m$ and a local order structure (Figure 5c). After 14 ZnS infiltration cycles, the

diffraction signal decreases (Figure 5d); after 28 ZnS infiltration cycles, a strong pattern typical of a highly ordered cubic $Im3m$ mesostructure is observed (Figure 5e). These results can be interpreted by taking into account the changes in the periodic electron density of the nanocomposites before and after infiltration. The decrease in scattering intensity observed for the first infiltration cycles can be explained in the basis of the decrease of electron density contrast between the MSF walls and the pores that take place upon partial pore filling. Scattering intensity can be lost upon partial loading due to the inhomogeneous distribution of the ZnS particles on the pore walls along the initial filling steps. In consequence, the initial SAXS pattern disappears but the original MSF mesostructure does not suffer any structural change as seen in the SEM images. When a higher loading of MSF with ZnS is achieved, the appearance of a cubic structure SAXS pattern is observed, due to the reappearing coherence in the periodic electron density structure. This fact is in excellent agreement with Figure 5b where a great fraction of the SiO₂ surface pores appear homogeneously filled with ZnS. In a previous work on Ag infiltration on mesoporous oxide matrices, the same SAXS signal disappearance was observed along pore filling with metallic nanoparticles.[40] In that case, the Ag nanoparticles were deposited following a random distribution along the mesoporous structure which in turn, disrupted the electronic periodic density. In this case, ZnS clusters grow homogeneously within the SiO₂ pores in a step by step fashion, ultimately leading to an inverse structure with a characteristic SAXS signal that keeps the symmetry of the mesopore system. It can be proposed that a small nanoparticle filling will blur the electronic density contrast; however, at higher loadings, the sulfide being significantly denser than silica (see below), a higher electronic contrast will result, and therefore, the X-ray scattering signal will be higher. A quantitative assessment of the ZnS loading is needed in order to understand this issue.

For a rigorous quantification of the ZnS loadings in the MSF, XRR measurements following previously published procedures were performed.[40] XRR signals depend on the electron density of the thin film, following the expression

$$\rho_{el} = \frac{\pi}{\lambda^2 r_e} \theta_c^2$$

(3)

where λ is the X-ray wavelength, r_e is the classical electron radius (2.813×10^{-6} nm), and θ_c is the critical angle at which total reflection of the X-ray takes place. The critical angle depends on the electron density of the film, and is distinguished as an abrupt decay in the XRR signal. Figure 6a shows a
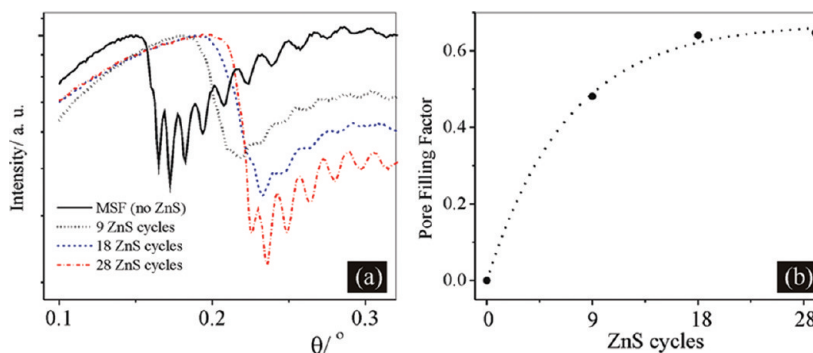

Figure 6. (a) Reflectivity data for the MSF prepared on ITO-covered glass substrate for different ZnS cycles and (b) pore filling factor with ZnS cycles.

progressive increase of θ_c with each SILAR cycle, due to the higher electronic density of the MSF:ZnS films along infiltration of the sulfide into the MSF pores.

The ZnS volume fraction at each infiltration step (F_{ZnS}) can be calculated from the critical angle variation, according to eq 4

$$F_{ZnS} = \frac{\rho_{NC} - \rho_{MSF}}{\rho_{ZnS}} \qquad (4)$$

where ρ_{NC} is the electronic density of the ZnS:MSF nanocomposite calculated from eq 3, ρ_{MSF} is the electronic density of the empty exotemplate, and ρ_{ZnS} is the ZnS electronic density, which was calculated as $\rho_{ZnS} = \delta_{ZnS}\, n_{ZnS}\, N_A / A_{ZnS}$ where $\delta_{ZnS} = 4.09$ g cm^{-3} is the ZnS mass density, n_{ZnS} is the ZnS atomic number, A_{ZnS} is the ZnS atomic mass, and N_A is Avogadro's number. The pore filling fraction (PFF) at each SILAR step can be calculated as shown in eq 5.

$$PFF = \frac{F_{ZnS}}{F_{MSF}} \qquad (5)$$

Typical PFF values for 9, 18, and 28 ZnS infiltration cycles are presented in Figure 6b, showing a plateau approximately at 20 ZnS infiltration cycles. This result corresponds to 60−65% of the pore relative volume, which is in good agreement with the results obtained from the UV/vis spectra. This limit of volume filling is similar to those found in nanoparticle-laden mesoporous systems, and might be due to partial blocking of the necks and pore clogging of the MSF as the number of infiltrations increases.[25]

Oscillations at angles higher than θ_c are due to the constructive interference of reflected X-rays on thin film interfaces and are known as XRR Kiessig fringes.[30,40,44] In the higher angle region ($\theta > 4\theta_c$) these periodic oscillations are related to the film thickness, d, according to

$$d = \frac{\lambda}{2\Delta(\sin\theta)} \qquad (6)$$

where λ is the wavelength of the monochromatic X-rays used and $\Delta(\sin\theta)$ is the period of these oscillations. Interestingly, no changes in $\Delta(\sin\theta)$ are observed in any of the 4 cases shown in Figure 6a, leading to the conclusion that the ZnS does not deposit as a top layer, but that the semiconductor is indeed deposited within the mesopore system. In addition, Kiessig fringes with a significantly lower amplitude are observed in the case of those samples submitted to 9 and 18 infiltration cycles with respect to the pristine MSF and the nanocomposite film after 24 infiltration cycles. This amplitude decrease followed by an increase is due to the loss of electronic contrast between the film and the substrate along partial filling, and subsequent contrast increase due to the presence of a high volume fraction occupied by ZnS, being consistent with the SAXS results of Figure 5c−e. In conclusion, a high ZnS loading of mesoporous silica thin films is achieved by the SILAR method reported here. An open issue is the ZnS growth mechanism, which can take place either by (a) heterogeneous ZnS nucleation on the pore surface in the first cycle followed by nanoparticle growth, (b) by successive nucleation−growth events on every cycle.

c. Dissolution of ZnS:MSF: toward Mesoporous ZnS Thin Films. Successful nanocasting procedures must rely on compatible chemistries for synthesis and dissolution of the exotemplate matrix. Usually, HF aqueous solutions are the typical etching agents for SiO_2; however, the ZnS structure might be damaged in the resulting low pH conditions. This

issue can be circumvented by using ethanolic HF in order to assist Si(IV) solubilization while keeping low ZnS solubility.[45,46,13] In this way, the SiO_2 exotemplate can be successfully etched away, leaving behind an intact mesoporous ZnS structure when using a 0.5% ethanolic HF solution. However, due to the similar chemical behavior of the glass substrates and the silica matrix, it is necessary to provide a buffer layer between the glass substrate and the MSF:ZnS to prevent the detachment of the mesoporous ZnS layer during this etching process. In summary, the etching method was chosen in such a way that neither the ITO nor ZrO_2 layers that covered the glass substrates nor the ZnS could be attacked by ethanolic HF.

Figure 7 shows four SEM images of MSF:ZnS samples after being exposed to the etching solution for different periods: 0, 5,
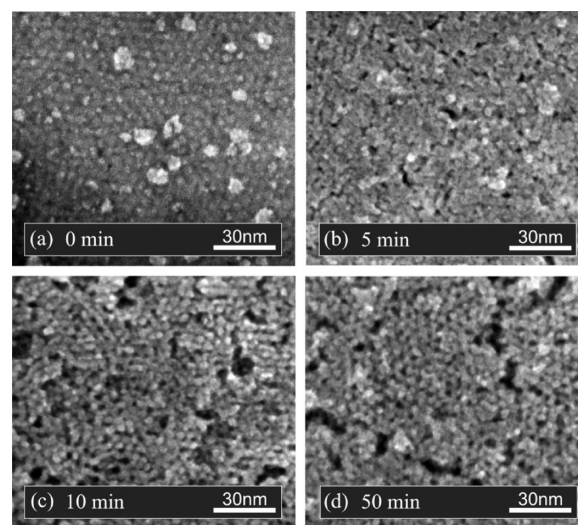

Figure 7. SEM images obtained from glass/ITO/SF:ZnS samples exposed to HF for (a) 0, (b) 5, (c) 10, and (d) 50 min.

10, and 50 min. Figure 7a corresponds to the MSF:ZnS thin film after 28 SILAR cycles and no etching process. After 5 min of exposure of the film to the HF solution, a partial dissolution of the SiO_2 matrix can be observed (Figure 7b) while loosely surface bound ZnS aggregates are also washed away. This dissolution continues along etching time, as shown in Figure 7c, d. The structure of the ZnS thin film remains unchanged to a large extent, and no detaching from the ITO covered glass substrate was observed neither by SEM nor visual inspection; indeed, ellipsometric porosimetry measurements (see below) were performed onto the ZnS films, confirming their integrity optical quality, thus their integrity.

The ZnS thin films etched for 0 and 50 min, were analyzed with SEM-EDS to obtain information about the SiO_2 content within the MSF:ZnS nanocomposite and the final mesoporous ZnS thin film. The corresponding SEM-EDS spectra, as well as the quantification of the elements are presented in Figure 8.

The nonetched MSF:ZnS film shows three strong EDS signals in the spectral maxima of Si, Zn and S, which correspond to the SiO_2 matrix (Si) and the ZnS infiltrated MSF (Zn and S), respectively. After 50 min etching with 0.5% ethanolic HF the Si peak in the SEM-EDS spectrum is hardly detectable, in contrast to the Zn and S signal, which are still present. This indicates that the SiO_2 matrix is successfully removed by the etching step. Moreover, when the SiO_2 framework is removed, a weak In peak arises from the ITO
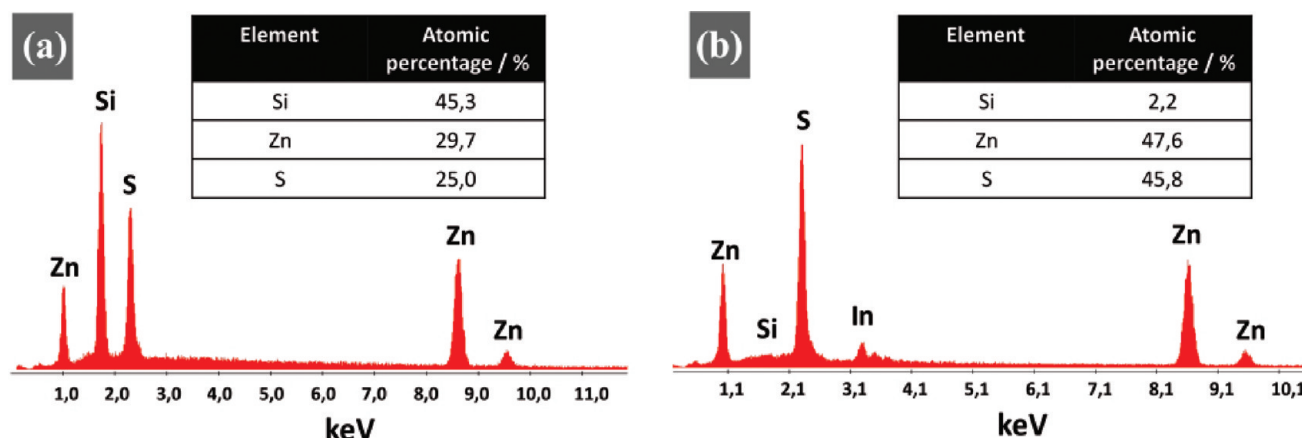
Figure 8. EDS spectra obtained from MSF:ZnS (28 infiltration cycles) exposed to ethanolic HF for (a) 0 and (b) 50 min. Samples were scraped off a glass/ITO substrate.
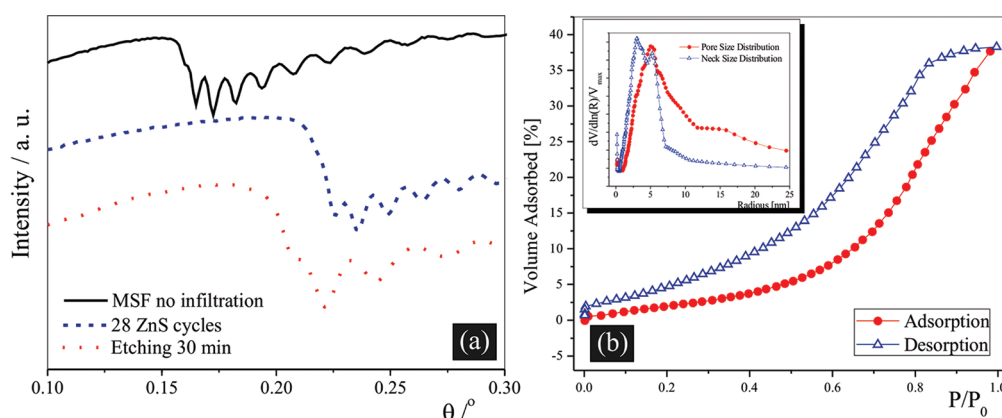

Figure 9. (a) XRR data for a not infiltrated MSF (black solid line), for the 28 ZnS infiltration cycle (blue dashed line) and for an etched ZnS film (red dotted line), (b) Adsorption−desorption isotherms for a 30-min etched ZnS film. Inset: pore and neck distribution.

layer of the glass/ITO substrate (Figure 8b); this is due to the lower density of the resulting porous ZnS film. In both cases, untreated and etched MSF:ZnS, the ratio between Zn and S is approximately 1:1, which corresponds well to the formation of ZnS.

In order to quantify the porosity of the ZnS mesoporous film after the etching process, the XRR technique was employed. Figure 9a shows the variation of the critical angle for the three main stages in the whole process. The black solid line shows a small θ_c for the not infiltrated MSF while an important increment of the θ_c is observed for the 28-cycle ZnS infiltrated film (blue dashed line), reflecting the increase in the electronic density of the nanocomposite, as already shown in Figure 6. After etching the SiO_2 matrix, a pronounced shift to a lower critical angle is observed, indicating that the electronic film density has decreased to a value between the empty MSF and the full MSF:ZnS, due to the removal of the SiO_2 exotemplate. As there are no representative changes in θ_c after 30 min, and considering the results obtained in the SEM-EDS measurements, it is possible to assume that almost all SiO_2 has been removed. Consequently, a ZnS mesoporous thin film has been obtained with an overall accessible porosity of approximately 45% calculated from XRR measurements (compared to dense ZnS).

Figure 9b shows the adsorption and desorption curves obtained by EEP for a ZnS film derived from 30 min etching of the silica film over ITO. An adsorbed volume of 38% is registered by this technique, in good agreement with the 45% obtained by XRR. The inset in Figure 9b shows the pore and neck size distribution obtained for this ZnS film. The corresponding isotherms show rather large pore size distributions, which correspond to different pore sizes, suggesting that the available porosity due to the removed SiO_2 generates different kind of channels in the film, as clearly showed in Figure 7. The pore size range presents relatively well-defined maxima at around 6 and 15 nm. From the data obtained from EEP technique it is also possible to determine that the film thickness decreases to 80 nm after etching, in agreement with the Kiessig fringes observable in Figure 9a, where the peak separation of the 30 min etched ZnS film (red dotted line) approximately doubles the one of the original film (black solid line). The incomplete filling of the original silica exotemplate (ca. 60% of the pore volume) leads to an open ZnS framework which is not totally connected. Upon etching of the silica exotemplate, the ZnS backbone can either reorganize or partially deteriorate, leading to a final thinner film. Efforts are being directed to address this issue in detail and will be communicated in a further publication. However, it must be stressed that the ZnS films obtained present accessible mesoporosity, optical homogeneity, and good adhesion to the ITO substrate.

Another important information obtained from EEP technique is the refractive index of mesoporous ZnS. EEP measurements show that under dry atmosphere (0%RH), n_{630}

= 1.57, increasing up to 1.74 when the material is exposed to 100% humidity. This significant increment of $\Delta n = 0.17$ implies that the film obtained is of potential interest for optical sensing applications.[47]

To obtain further structural information about the mesoporous ZnS, the thin film was studied by TEM and selected area electron diffraction. Figure 10a shows a TEM
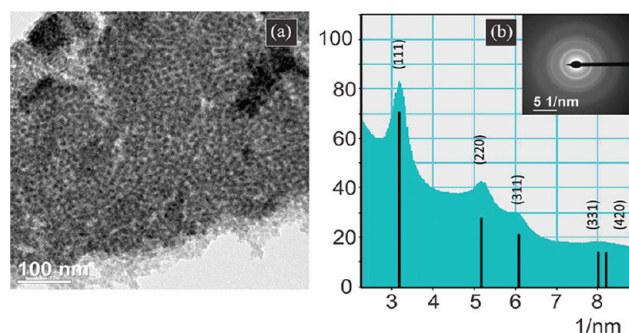

Figure 10. (a) TEM image and (b) electron diffraction analysis and diffraction rings of a mesoporous ZnS thin film scratched off a glass/ITO substrate after removal of the SiO$_2$ matrix. Black lines give the position of the peaks according to the powder diffraction file (PDF) 05−05665 of the International Centre for Diffraction Data for sphalerite type ZnS.

image recorded from a mesoporous ZnS thin film scratched from a glass/ITO substrate, obtained after etching in ethanolic HF solution for 50 min. The ZnS pores show a long-range order, which is consistent with recorded SEM images of the MSF:ZnS films. SAED analysis was evaluated by using the method described by Mitchell (Figure 10b).[48] The electron diffraction pattern shows five well resolved main rings, corresponding to the diffraction of different planes of the randomly ordered nanocrystallites. The positions of the rings can be assigned to sphalerite type ZnS, which is in accordance with the Powder Diffraction File (PDF) 05−05665. In this way, a robust mesoporous nanocrystalline ZnS can be deposited onto a semiconductor substrate. Moreover, the mesoporous ZnS thin film reported here shows photoluminescence (see the Supporting Information); further studies are under way to delve with these properties.

CONCLUSIONS

In this contribution, we present the successful preparation of organized mesoporous ZnS thin layers using a nanocasting approach. The SiO$_2$ exotemplate prepared by evaporation induced self-assembly process using an F-127 polymeric template is highly accessible and thus acts as an adequate exotemplating agent, facilitating the infiltration of the MSF matrix with ZnS. The SILAR route proves to be a useful approach to build nonoxide mesoporous nanophases, due to the high control of the ion infiltration-surface precipitation processes that are mainly confined in the pore interior. This strategy relies on the control of several phenomena taking place in the mesoporous exotemplate material upon loading of the precursors of the desired phase, and the further confined growth of said phase. In the first place, pore charge, size and interconnectivity are extremely important, for they determine the affluence and organized deposition of the precursors; these effects are key for example in perm-selectivity, or controlled transport.[49] Indeed, the controlled synthesis presented here

demonstrates that these confinement-dependent properties (a central feature of mesoporous systems) can be exploited as a synthetic tool.[50] In the subsequent filling step, the exotemplate removed by exposing the film to an ethanolic HF solution yields a stable and nearly SiO$_2$-free mesoporous ZnS thin film on a transparent electrode such as a glass/ITO substrate. The sequential strategy presented here can be extended in principle to more complex materials, in particular to sulfides or selenides, such as Cu(In,Ga)Se$_2$ (CIGS) or related phases that present high interest in solar cells. The combination of these robust and highly accessible nanostructured materials with metals or conductive polymers[51] can lead to new developments for sensors or heterogeneous junctions used in inorganic−organic hybrid photovoltaics.

ASSOCIATED CONTENT

S Supporting Information

Photoluminescence spectra of mesoporous ZnS thin films is provided. This material is available free of charge via the Internet at http://pubs.acs.org/.

AUTHOR INFORMATION

Corresponding Author

*E-mail: gsoler@cnea.gov.ar. Tel.: 0054 9 11 6507 1916.

Notes

The authors declare no competing financial interest.

ACKNOWLEDGMENTS

REFERENCES

(1) Kresge, C. T.; Leonowicz, M. E.; Roth, W. J.; Vartuli, J. C.; Beck, J. S. *Nature* **1992**, *359*, 710−712.

(2) Yanagisawa, T.; Shimizu, T.; Kuroda, K.; Kato, C. *Bull. Chem. Soc. Jpn.* **1990**, *63*, 988−992.

(3) Ding, Y.; Chen, M.; Erlebacher, J. *J. Am. Chem. Soc.* **2004**, *126*, 6876−6877.

(4) Hu, J. S.; Ren, L. L.; Guo, Y. G.; Liang, H. P.; Cao, A. M.; Wan, L. J.; Bai, C. L. *Angew. Chem., Int. Ed.* **2005**, *44*, 1269−1273.

(5) Reddy, K. M.; Satyanarayana, L.; Manorama, S. V.; Misra, R. D. K. *Mater. Res. Bull.* **2004**, *39*, 1491−1498.

(6) Li, J.; Kessler, H.; Soular, M.; Khouchaf, L.; Tuilier, M.-H. *Adv. Mater.* **1998**, *10*, 946−949.

(7) Nistor, L. C.; Mateescu, C. D.; Birjega, R.; Nistor, S. V. *Appl. Phys. A: Mater. Sci. Process.* **2008**, *92*, 295−301.

(8) Braun, P. V.; Osenar, P.; Tohver, V.; Kennedy, S. B.; Stupp, S. I. *J. Am. Chem. Soc.* **1999**, *121*, 7302−7309.

(9) Rana, R. K.; Zhang, L.; Yu, J. C.; Mastai, Y.; Gedanken, A. *Langmuir* **2003**, *19*, 5904−5911.

(10) Braun, P. V.; Osenar, P.; Twardowski, M.; Tew, G. N.; Stupp, S. I. *Adv. Funct. Mater.* **2005**, *15*, 1745−1750.

(11) Van Gough, D.; Wolosiuk, A.; Braun, P. V. *Nano Lett.* **2009**, *9*, 1994−1998.

(12) Wolosiuk, A.; Armagan, O.; Braun, P. V. *J. Am. Chem. Soc.* **2005**, *127*, 16356−16357.

(13) Son, D.; Wolosiuk, A.; Braun, P. V. *Chem. Mater.* **2009**, *21*, 628−634.

(14) Schüth, F. *Chem. Mater.* **2001**, *13*, 3184−3195.

(15) Karakaya, C.; Türker, Y.; Albayrak, C.; Dag, O. *Chem. Mater.* **2011**, *23*, 3062−3071.

(16) Türker, Y.; Karakaya, C.; Dag, Ö. *Chem.—Eur. J.* **2012**, *18*, 3695−3705.

(17) Lepoutre, S.; Julián-López, B.; Sanchez, C.; Amenitsch, H.; Linden, M.; Grosso, D. *J. Mater. Chem.* **2010**, *20*, 537−542.

(18) Yang, H.; Zhao, D. *J. Mater. Chem.* **2005**, *15*, 1217−1231.

(19) Flath, J.; Meldrum, F. C.; Knoll, W. *Thin Solid Films* **1998**, *327−329*, 506−509.

(20) Kosmulski, M. *Chemical Properties of Material Surfaces*; CRC: Boca Raton, FL, 2001; Vol. *102*.

(21) Tiemann, M. *Chem.—Eur. J.* **2007**, *13*, 8376−8388.

(22) Waitz, T.; Wagner, T.; Sauerwald, T.; Kohl, C. D.; Tiemann, M. *Adv. Funct. Mater.* **2009**, *19*, 653−661.

(23) Valdés-Solís, T.; Fuertes, A. B. *Mater. Res. Bull.* **2006**, *41*, 2187−2197.

(24) Schüth, F. *Angew. Chem., Int. Ed.* **2003**, *42*, 3604−3622.

(25) Lepoutre, S.; Smått, J.-H.; Laberty, C.; Amenitsch, H.; Grosso, D.; Lindén, M. *Microporous Mesoporous Mater.* **2009**, *123*, 185−192.

(26) Grosso, D.; Cagnol, F.; Soler-Illia, G. J. D. A. A.; Crepaldi, E. L.; Amenitsch, H.; Brunet-Bruneau, A.; Bourgeois, A.; Sanchez, C. *Adv. Funct. Mater.* **2004**, *14*, 309−322.

(27) Nicolau, Y. F. *Appl. Surf. Sci.* **1985**, *22−23*, 1061−1074.

(28) Niesen, T. P.; De Guire, M. R. *Solid State Ionics* **2002**, *151*, 61−68.

(29) Ristov, M.; Sinadinovski, G.; Grozdanov, I.; Mitreski, M. *Thin Solid Films* **1989**, *173*, 53−58.

(30) van der Lee, A. *Solid State Sci.* **2000**, *2*, 257−278.

(31) Angelome, P. C.; Fuertes, M. C.; Soler-Illia, G. *Adv. Mater.* **2006**, *18*, 2397-+.

(32) Bass, M.; Mahajan, V. N.; Van Stryland, E. *Handbook of Optics: Design, Fabrication, and Testing; Sources and Detectors; Radiometry and Photometry*; McGraw-Hill Professional: New York, 2009; Vol. *4*.

(33) Synowicki, R. A. *Thin Solid Films* **1998**, *313−314*, 394−397.

(34) Boissiere, C.; Grosso, D.; Lepoutre, S.; Nicole, L.; Bruneau, A. B.; Sanchez, C. *Langmuir* **2005**, *21*, 12362−12371.

(35) Kruk, M.; Jaroniec, M. *Chem. Mater.* **2003**, *15*, 2942.

(36) Lowell, S.; Shields, J. E.; Thomas, M. A.; Thommes, M. *Characterization of Porous Solids and Powders: Surface Area, Porosity and Density*; Springer: New York, 2006.

(37) Galarneau, A.; Desplantier, D.; Dutartre, R.; Di Renzo, F. *Microporous Mesoporous Mater.* **1999**, *27*, 297−308.

(38) Sakatani, Y.; Grosso, D.; Nicole, L.; Boissière, C.; Soler-Illia, G. J. D. A. A.; Sanchez, C. *J. Mater. Chem.* **2006**, *16*, 77−82.

(39) Brunsen, A.; Calvo, A.; Williams, F. J.; Soler-Illia, G. J. A. A.; Azzaroni, O. *Langmuir* **2011**, *27*, 4328−4333.

(40) Fuertes, M. C.; Marchena, M.; Marchi, M. C.; Wolosiuk, A.; Soler-Illia, G. *Small* **2009**, *5*, 272−280.

(41) Nicolau, Y. F.; Dupuy, M.; Brunel, M. *J. Electrochem. Soc.* **1990**, *137*, 2915−2924.

(42) Rossetti, R.; Hull, R.; Gibson, J. M.; Brus, L. E. *J. Chem. Phys.* **1985**, *82*, 552−559.

(43) Hodes, G. *Chemical Solution Deposition of Semiconductor Films*; CRC Press: Boca Raton, FL, 2003.

(44) Gibaud, A.; Hazra, S. *Curr. Sci.* **2000**, *78*, 1467−1477.

(45) Ràfols, C.; Herodes, K.; Beltrán, J. L.; Bosch, E.; Rosés, M. *J. Electroanal. Chem.* **1997**, *433*, 77−83.

(46) Velikov, K. P.; Van Blaaderen, A. *Langmuir* **2001**, *17*, 4779−4786.

(47) Fuertes, M. C.; López-Alcaraz, F. J.; Marchi, M. C.; Troiani, H. E.; Luca, V.; Míguez, H.; Soler-Illia, G. J. D. A. A. *Adv. Funct. Mater.* **2007**, *17*, 1247−1254.

(48) Mitchell, D. R. G. *Ultramicroscopy* **2008**, *108*, 367−374.

(49) Schoch, R. B.; Han, J.; Renaud, P. *Rev. Mod. Phys.* **2008**, *80*, 839−883.

(50) Calvo, A.; Fuertes, M. C.; Yameen, B.; Williams, F. J.; Azzaroni, O.; Soler-Illia, G. J. A. A. *Langmuir* **2010**, *26*, 5559−5567.

(51) Soler-Illia, G. J. A. A.; Azzaroni, O. *Chem. Soc. Rev.* **2011**, *40*, 1107−1150.